

## Article

# Calcium Ferrite Nanoparticles: A Simple Synthesis Approach for the Effective Disposal of Congo Red Dye from Aqueous Environments

Nada S. Al-Kadhi <sup>1</sup>, Ghadah M. Al-Senani <sup>1</sup>, Faisal K. Algethami <sup>2</sup>, Reem K. Shah <sup>3</sup>, Fawaz A. Saad <sup>3</sup>, Alaa M. Munshi <sup>3</sup>, Khalil ur Rehman <sup>4</sup>, Lotfi Khezami <sup>2</sup> and Ehab A. Abdelrahman <sup>2,5,\*</sup>

<sup>1</sup> Department of Chemistry, College of Science, Princess Nourah bint Abdulrahman University, P.O. Box 84428, Riyadh 11671, Saudi Arabia; nsalkadhi@pnu.edu.sa (N.S.A.-K.); gmalsnany@pnu.edu.sa (G.M.A.-S.)

<sup>2</sup> Department of Chemistry, College of Science, Imam Mohammad Ibn Saud Islamic University (IMSIU), Riyadh 11623, Saudi Arabia

<sup>3</sup> Department of Chemistry, Faculty of Science, Umm Al-Qura University, Makkah 21955, Saudi Arabia

<sup>4</sup> Institute of Chemical Sciences, Gomal University, Dera Ismail Khan 29111, KPK, Pakistan

<sup>5</sup> Chemistry Department, Faculty of Science, Benha University, Benha 13518, Egypt

\* Correspondence: eaaahmed@imamu.edu.sa

**Abstract:** Congo red dye is classified as a toxic chemical and can be harmful if ingested, inhaled, or in contact with the skin or eyes. It can cause irritation, allergic reactions, and skin sensitization in some individuals. Thus, in this paper,  $\text{CaFe}_2\text{O}_4$  nanoparticles were produced by a simple Pechini sol-gel approach and used as an adsorbent material for the efficient disposal of Congo red dye from aqueous solutions. The maximum adsorption capacity of the  $\text{CaFe}_2\text{O}_4$  towards Congo red dye is 318.47 mg/g. Furthermore, the synthesized  $\text{CaFe}_2\text{O}_4$  nanoparticles exhibit an average crystal size of 24.34 nm. Scanning electron microscopy (SEM) examination showed that the  $\text{CaFe}_2\text{O}_4$  nanoparticles are basically ball-like particles with a mean grain size of 540.54 nm. Moreover, transmission electron microscopy (TEM) examination showed that the  $\text{CaFe}_2\text{O}_4$  sample revealed aggregated spherical particles with a mean diameter of 27.48 nm. The Energy-dispersive X-ray spectroscopy (EDS) pattern reveals that the produced  $\text{CaFe}_2\text{O}_4$  nanoparticles are composed of Ca, Fe, and O elements, with an atomic ratio of 1:2:4 of these elements, respectively. The disposal of Congo red dye by the synthesized  $\text{CaFe}_2\text{O}_4$  nanoparticles is chemical, spontaneous, exothermic, perfectly aligned with the pseudo-second-order kinetic model, and exhibited excellent conformity with the Langmuir equilibrium isotherm.

**Keywords:** adsorption; Congo red dye;  $\text{CaFe}_2\text{O}_4$  nanoparticles; characterization



**Citation:** Al-Kadhi, N.S.; Al-Senani, G.M.; Algethami, F.K.; Shah, R.K.; Saad, F.A.; Munshi, A.M.; Rehman, K.u.; Khezami, L.; Abdelrahman, E.A. Calcium Ferrite Nanoparticles: A Simple Synthesis Approach for the Effective Disposal of Congo Red Dye from Aqueous Environments. *Inorganics* **2024**, *12*, 69. <https://doi.org/10.3390/inorganics12030069>

Academic Editor: Chiara Dionigi

Received: 27 January 2024

Revised: 22 February 2024

Accepted: 22 February 2024

Published: 24 February 2024



**Copyright:** © 2024 by the authors. Licensee MDPI, Basel, Switzerland. This article is an open access article distributed under the terms and conditions of the Creative Commons Attribution (CC BY) license (<https://creativecommons.org/licenses/by/4.0/>).

## 1. Introduction

Wastewater discharged from various industrial sectors, including textiles, paper production, rubber manufacturing, food coloring, cosmetics, and others, often contains significant quantities of harmful dyes [1–3]. If these effluents are released into natural water bodies, they can lead to severe water pollution. Wastewater containing dyes can elevate the chemical oxygen demand in water and diminish light penetration, affecting the photosynthesis activity in aquatic environments [4,5]. Certain dyes are non-biodegradable due to their intricate aromatic structure and can be carcinogenic and mutagenic to humans [6]. Congo red dye, like many other synthetic dyes, can pose potential dangers to both humans and the environment. Some studies have suggested that certain dyes, including Congo red, may have carcinogenic properties and could be linked to cancer when exposure occurs at high levels over extended periods. Congo red and other similar dyes have been associated with mutagenic effects, potentially causing DNA damage, which can lead to genetic mutations and diseases. Contact with Congo red dye may cause skin and eye

irritation, leading to discomfort and potential health issues [7,8]. The adverse impacts of synthetic dyes have prompted environmental researchers to explore innovative methods and materials for their secure and efficient elimination from water sources. Hence, various chemical, microbiological, and physical methods, including photodegradation, chemical oxidation/precipitation, coagulation, microbiological degradation, and adsorption, have been employed to purify wastewater contaminated with dyes [9–13]. Among the numerous methods for treating dye contamination, adsorption stands out as a highly efficient technique, owing to the abundance of available adsorbents, its ease of operation, cost-effectiveness, and superior efficiency [14–16]. A diverse range of adsorbents, including activated carbon, metal–organic frameworks (MOFs), zeolites, and polymers, have been investigated for the removal of dyes from aqueous media [17–20]. Nonetheless, several of these adsorbents exhibit limitations such as limited adsorption capacity, high cost, poor regeneration capabilities, and slow adsorption rates, among other drawbacks. Metal oxide nanoparticles play a crucial role in the adsorption of organic dyes due to their unique properties and surface characteristics. These nanoparticles possess a high surface area and abundant surface functional groups, making them excellent adsorbents for organic dyes. Their small size allows for efficient interaction with dye molecules, leading to enhanced adsorption capacity. Furthermore, the high stability and recyclability of metal oxide nanoparticles make them environmentally friendly and economically viable options for wastewater treatment processes, contributing significantly to the removal of organic dyes from contaminated water sources. Metal ferrite nanoparticles, such as  $\text{MnFe}_2\text{O}_4$ ,  $\text{ZnFe}_2\text{O}_4$ ,  $\text{CoFe}_2\text{O}_4$ , and  $\text{MgFe}_2\text{O}_4$ , have garnered substantial attention for their utility as effective adsorbents in the disposal of heavy metals and dyes from aqueous environments [21–29]. Metal ferrite adsorbents are typically favored because of their compact dimensions, high surface area, and substantial pore volume, which facilitate a quicker disposal process and enhance disposal capacity when contrasted with traditional adsorbents. Furthermore, metal ferrite adsorbents possess magnetic characteristics that provide another benefit, simplifying their extraction from aqueous environments. This property promotes effortless recyclability and diminishes operational expenses. In this study, the adsorption efficacy of magnetic calcium ferrite nanoparticles for the disposal of Congo red dye from aqueous environments was examined. The  $\text{CaFe}_2\text{O}_4$  nanoparticles were synthesized using a simple Pechini sol-gel method and characterized using several tools to identify their morphology, crystal structure, and the functional chemical groups located on their surface. A comprehensive investigation into the impact of several experimental factors, such as reaction time, solution pH, initial dye concentration, and reaction temperature, on the disposal efficiency of Congo red dye was conducted. Furthermore, kinetic and isotherm modelling techniques were used for the adsorption data to gain a deeper understanding of the removal process. Moreover, to comprehend the effect of temperature on the disposal of Congo red dye by  $\text{CaFe}_2\text{O}_4$  nanoparticles, a thermodynamic study was conducted. Also, the effects of regeneration and reusability were studied.

## 2. Experimental

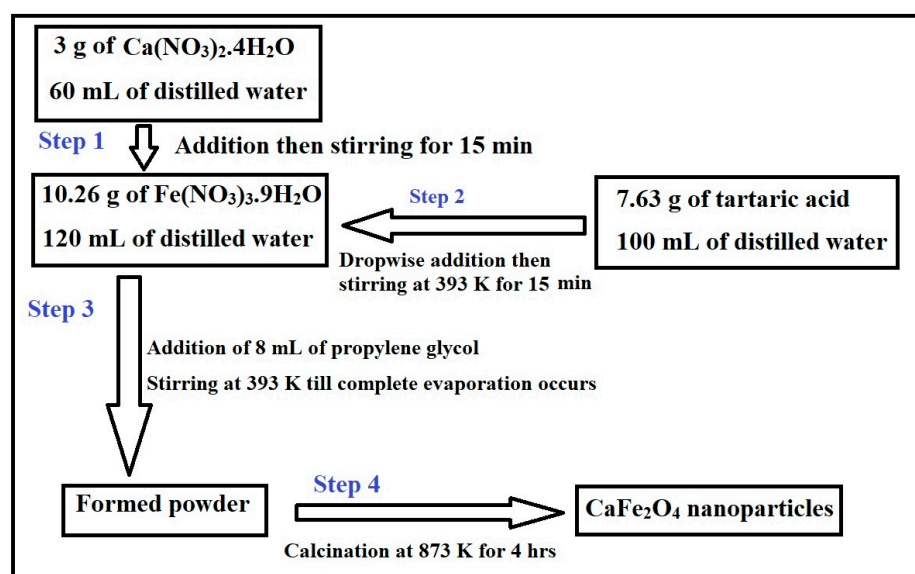
### 2.1. Materials

Calcium(II) nitrate tetrahydrate ( $\text{Ca}(\text{NO}_3)_2 \cdot 4\text{H}_2\text{O}$ ), iron(III) nitrate nonahydrate ( $\text{Fe}(\text{NO}_3)_3 \cdot 9\text{H}_2\text{O}$ ), potassium nitrate ( $\text{KNO}_3$ ), tartaric acid ( $\text{C}_4\text{H}_6\text{O}_6$ ), hydrochloric acid ( $\text{HCl}$ ), propylene glycol ( $\text{C}_3\text{H}_8\text{O}_2$ ), sodium hydroxide ( $\text{NaOH}$ ), and Congo red dye ( $\text{C}_{32}\text{H}_{22}\text{N}_6\text{Na}_2\text{O}_6\text{S}_2$ ) were supplied by the Sigma Aldrich Company (St. Louis, MO, USA). In addition, all chemicals were of analytical grade and were utilized without further purification.

### 2.2. Synthesis of $\text{CaFe}_2\text{O}_4$ Nanoparticles

The chemical solution of Ca(II) ions was freshly synthesized by dissolving 3.00 g of calcium(II) nitrate tetrahydrate in 60 mL of distilled water. Additionally, the chemical solution of Fe(III) ions was freshly synthesized by dissolving 10.26 g of iron(III) nitrate

nonahydrate in 120 mL of distilled water. Afterward, the solution of Ca(II) ions was added to the solution of Fe(III) ions; then, the produced blend was regularly stirred at room temperature for 15 min with a magnetic stirrer. Furthermore, the tartaric acid solution, which was synthesized by dissolving 7.63 g of tartaric acid powder in 100 mL of distilled water, was dropwise added as a complexing agent; then, the produced blend was regularly stirred at 393 K for 15 min using a magnetic stirrer. Afterward, 8 mL of propylene glycol was dropwise added as a crosslinker; then, the produced blend was regularly stirred at 393 K using a magnetic stirrer until complete evaporation occurred. The obtained powder underwent a calcination process at 873 K for 4 h. After the calcination process, the product was ground well using a pestle and mortar to acquire the powdered state of calcium ferrite nanoparticles. Scheme 1 summarizes the previous practical steps for the production of  $\text{CaFe}_2\text{O}_4$  nanoparticles.



**Scheme 1.** The practical steps for the production of  $\text{CaFe}_2\text{O}_4$  nanoparticles.

### 2.3. Characterization

A Bruker D8 Advance X-ray diffractometer (Billerica, MA, USA) was employed to analyze the X-ray diffraction (XRD) pattern of  $\text{CaFe}_2\text{O}_4$  powder. This analysis covered the  $2\theta$  range from  $5^\circ$  to  $80^\circ$ , utilizing  $\text{Cu K}\alpha$  radiation featuring a wavelength of 0.154178 nm. A field emission scanning electron microscope (FESEM, TESCAN model Vega 3, Brno, Czech Republic) was used for conducting surface morphological investigations. The FTIR spectrum of  $\text{CaFe}_2\text{O}_4$  powder was acquired using an FTIR spectrometer (Perkin Elmer, Waltham, MA, USA). Transmission electron microscopy (TEM, JEOL Ltd. model JEOLJEM 2100, Tokyo, Japan) was used for studying morphology. For the determination of the BET surface area and total pore volume of the  $\text{CaFe}_2\text{O}_4$  nanoparticles, an  $\text{N}_2$  gas analyzer (Quantachrome, Nova 2000, Graz, Austria) was used. The magnetic properties of the  $\text{CaFe}_2\text{O}_4$  nanoparticles were determined at  $25^\circ\text{C}$  using a vibrating sample magnetometer (VSM-Cryogenic Limited PPMS, San Diego, California, United States).

### 2.4. Removal of Congo Red Dye from Aqueous Media

In a dark place, 0.05 g of  $\text{CaFe}_2\text{O}_4$  adsorbent was separately added into 100 mL of 200 mg/L Congo red dye solutions. After that, the pH of the blend was studied in the range of 2–10, and then the blend was regularly agitated at 500 rpm for 180 min using a magnetic stirrer. Additional experiments were conducted to investigate the effect of contact time (10–120 min) at pH 2, as previously described. Further experiments were conducted to investigate the effect of adsorption temperature (298–328 K) at pH 2 and 80 min, as previously reported. Moreover, additional experiments were conducted to investigate the

effect of the initial Congo red concentration (50–250 mg/L) at pH 2, 298 K, and 80 min, as previously described. After the adsorption experiments were completed, the  $\text{CaFe}_2\text{O}_4$  adsorbent was separated from the Congo red dye solution utilizing an external magnetic field, and the supernatant was subjected to analysis for any remaining dye concentration. This analysis was performed utilizing a UV–Vis spectrophotometer (Shimadzu 1800 series, Kyoto, Japan), with measurements carried out at the maximum Congo red dye wavelength (i.e., 497 nm). Sometimes slight shifts in maximum wavelength occur when the pH changes; in this case, they were taken into account, and measurements were taken at the new maximum wavelength.

The disposal percentage of Congo red dye (% R) and the adsorption capacity of the  $\text{CaFe}_2\text{O}_4$  adsorbent ( $Q$ , mg/g) were determined utilizing Equations (1) and (2), respectively [14–16,30–34].

$$\% R = \frac{C_o - C_e}{C_o} \times 100 \quad (1)$$

$$Q = (C_o - C_e) \times \frac{V}{M} \quad (2)$$

where  $C_o$  is the initial concentration of Congo red dye (mg/L),  $C_e$  is the equilibrium concentration of Congo red dye (mg/L),  $M$  is the dry mass of the  $\text{CaFe}_2\text{O}_4$  adsorbent (g), and  $V$  is the volume of the Congo red dye solution (L).

The point of zero charge ( $\text{pH}_{\text{PZC}}$ ) for the  $\text{CaFe}_2\text{O}_4$  adsorbent was determined using the salt addition procedure [35]. A series of 50 mL conical flasks, each including 25 mL of a 0.01 M  $\text{KNO}_3$  solution, were prepared so that the initial pH ( $\text{pH}_i$ ) values ranged from 2.50 to 11.50. The pH of these solutions was altered by 0.1 M HCl or NaOH. Afterward, 0.03 g of  $\text{CaFe}_2\text{O}_4$  adsorbent was introduced into each flask. The solid/liquid mixtures were thoroughly mixed and regularly stirred for 6 h. After the solutions were separated, the final pH ( $\text{pH}_f$ ) of the filtrates was measured. By plotting  $\text{pH}_f$  against  $\text{pH}_i$ , the  $\text{pH}_{\text{PZC}}$  was determined as the  $\text{pH}_f$  value at which a unique stage was noticed.

### 3. Results and Discussion

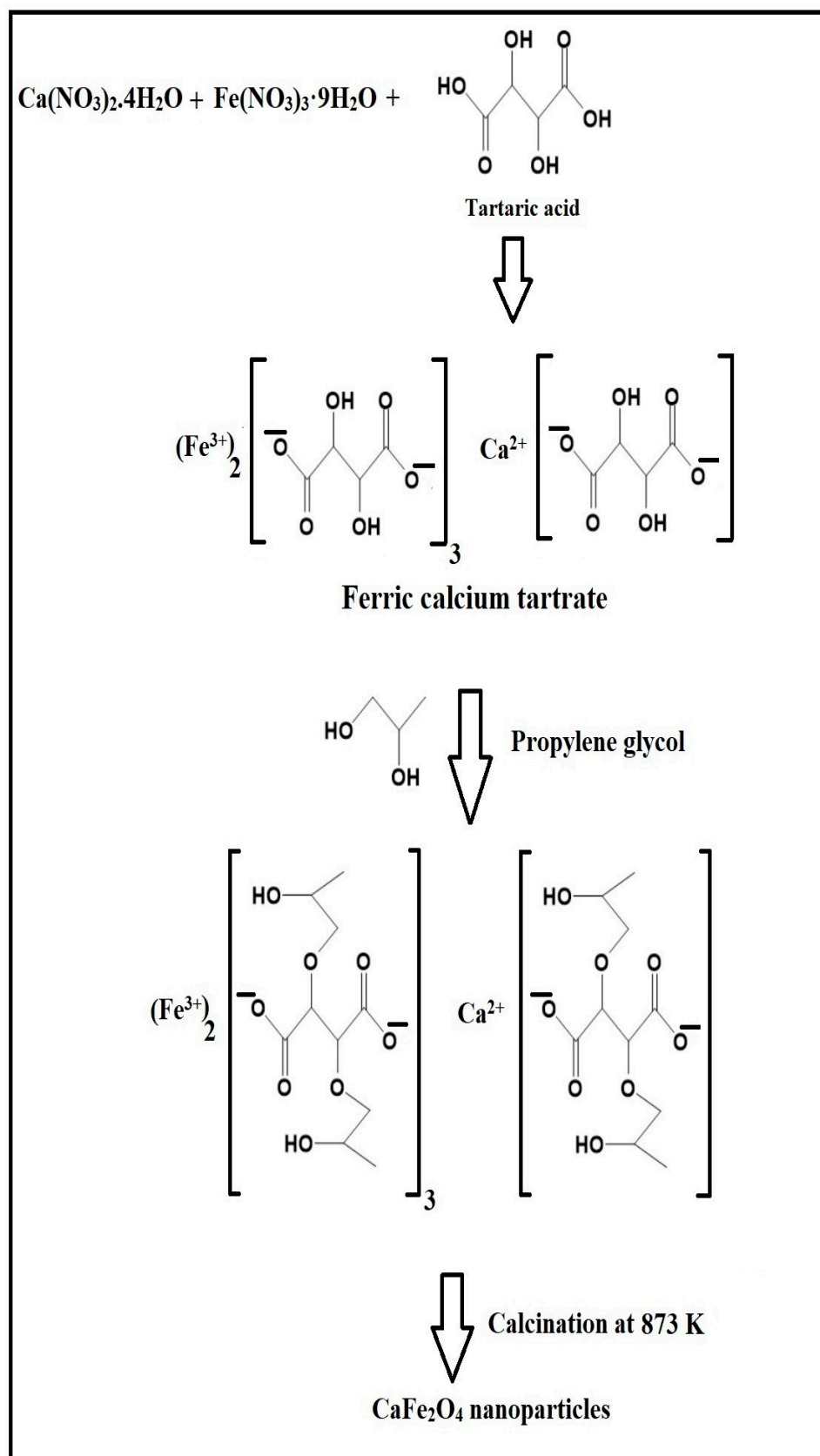
#### 3.1. Synthesis and Characterization of $\text{CaFe}_2\text{O}_4$ Nanoparticles

The  $\text{CaFe}_2\text{O}_4$  nanoparticles were produced by the Pechini sol-gel method, as presented in Scheme 2. The ferric calcium tartrate/propylene glycol network was formed by the reaction of  $\text{Fe}(\text{NO}_3)_3 \cdot 9\text{H}_2\text{O}$  and  $\text{Ca}(\text{NO}_3)_2 \cdot 4\text{H}_2\text{O}$  with tartaric acid and propylene glycol. After that, the mixture was heated at 393 K until dryness, and then the formed powder was calcinated at 873 K for 4 h to obtain  $\text{CaFe}_2\text{O}_4$  nanoparticles.

Figure 1 represents the thermal gravimetric analysis of the formed powder before the calcination process. The sample displayed a decomposition pattern with three steps. The first step, which is located in the range from 298 K to 463 K, can be attributed to the loss of adsorbed water molecules, with a weight loss of 14%. The second and third steps, which are located in the range from 463 K to 873 K, can be attributed to the loss of organic moiety, with a weight loss of 59%. It is evident that 873 K is the optimal temperature for the formation of  $\text{CaFe}_2\text{O}_4$  nanoparticles, as there is no weight loss after 873 K.

An X-ray diffraction (XRD) analysis was conducted on the uncalcinated and calcinated samples to look into their crystalline structure and phase composition, as shown in Figure 2A,B, respectively. The XRD pattern of the uncalcinated sample shows a broad band at  $2\theta = 21^\circ$  and does not show sharp crystalline diffraction peaks due to its amorphous nature. In contrast, the X-ray diffraction (XRD) pattern of the calcinated sample corresponded most accurately to the orthorhombic crystal unit cell with space group  $\text{Pnma}$  and lattice parameters  $a = 9.213 \text{ \AA}$ ,  $b = 10.695 \text{ \AA}$ , and  $c = 3.002 \text{ \AA}$ . The (hkl) planes seen in the XRD pattern of the calcinated sample were very similar to those in the orthorhombic  $\text{CaFe}_2\text{O}_4$  profile, which can be found in JCPDS No. 72-1199 [36]. Prominent peaks were observed at  $2\theta$  values of  $29.17^\circ$ ,  $34.31^\circ$ ,  $41.66^\circ$ ,  $51.62^\circ$ ,  $54.97^\circ$ ,  $60.96^\circ$ , and  $75.50^\circ$ , which corresponded to reflections from various Miller planes of  $\text{CaFe}_2\text{O}_4$ , including (310), (121), (150), (151), (431),

(620), and (601), respectively. The average crystallite size, which was determined by the Scherrer equation [37], of the  $\text{CaFe}_2\text{O}_4$  nanoparticles was determined to be 24.34 nm.



**Scheme 2.** Synthesis of  $\text{CaFe}_2\text{O}_4$  nanoparticles by the Pechini sol-gel method.

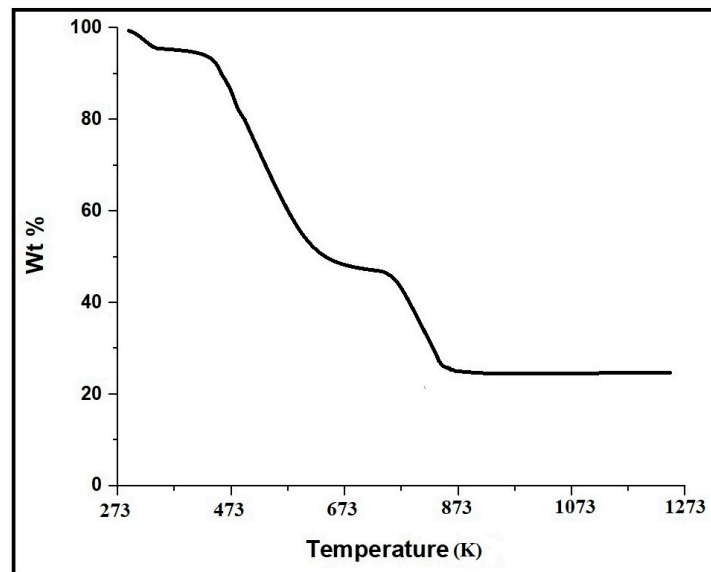


Figure 1. Thermal gravimetric analysis of the formed powder before the calcination process.

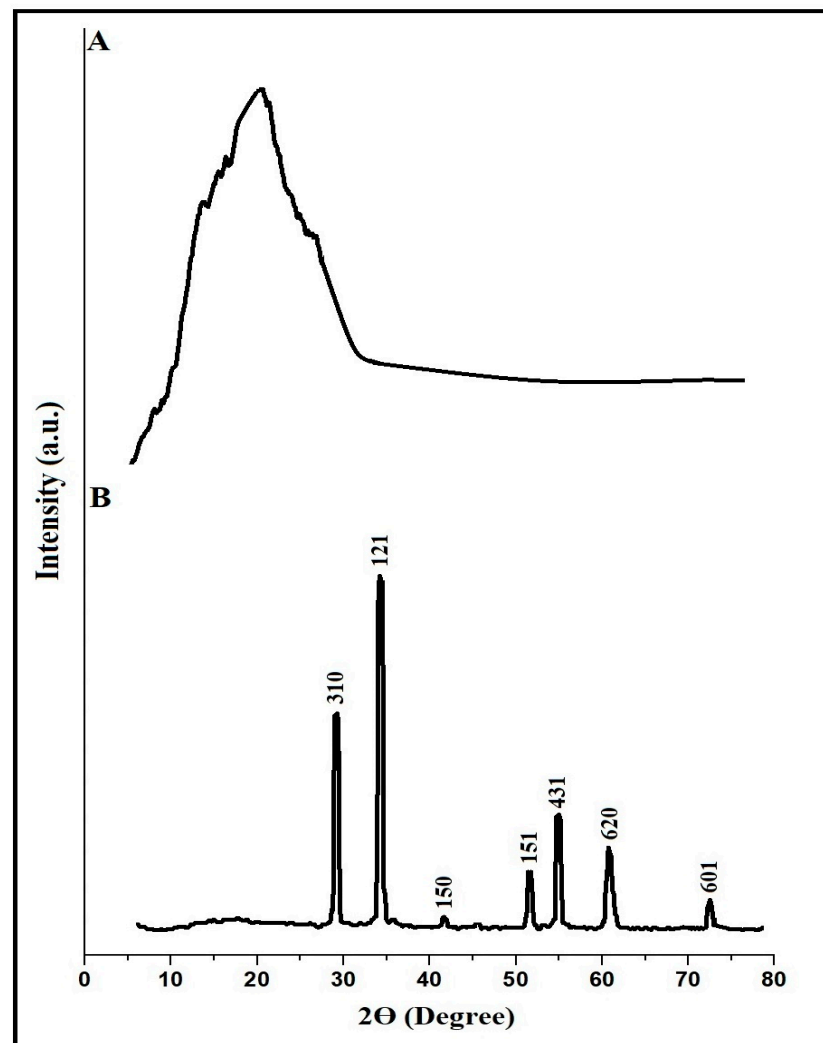


Figure 2. XRD analysis of the uncalcinated (A) and calcinated (B) samples.

A Fourier-transform infrared spectroscopy (FTIR) analysis was conducted on the uncalcinated and calcinated samples to look into their functional chemical bonds, as shown in Figure 3A,B, respectively. The bands that appeared in the uncalcinated sample at 445 and 572  $\text{cm}^{-1}$  and in the calcinated sample at 449 and 576  $\text{cm}^{-1}$  are due to the stretching vibrations of Fe-O and Ca-O, respectively. The bands that appeared in the uncalcinated sample at 1634 and 3510  $\text{cm}^{-1}$  and in the calcinated sample at 1634 and 3449  $\text{cm}^{-1}$ , are due to the bending and stretching vibrations of OH, respectively. In the Pechini sol-gel method, residual hydroxyl groups may remain bonded to the surface of the resulting oxide material, which explains the presence of hydroxyl after the calcination. The bands that appeared in the uncalcinated sample at 1747 and 2859  $\text{cm}^{-1}$  are due to the stretching vibrations of C=O and CH, respectively [36,38,39]. These peaks disappeared in the calcinated sample as a result of their elimination during calcination and the formation of  $\text{CaFe}_2\text{O}_4$  nanoparticles.

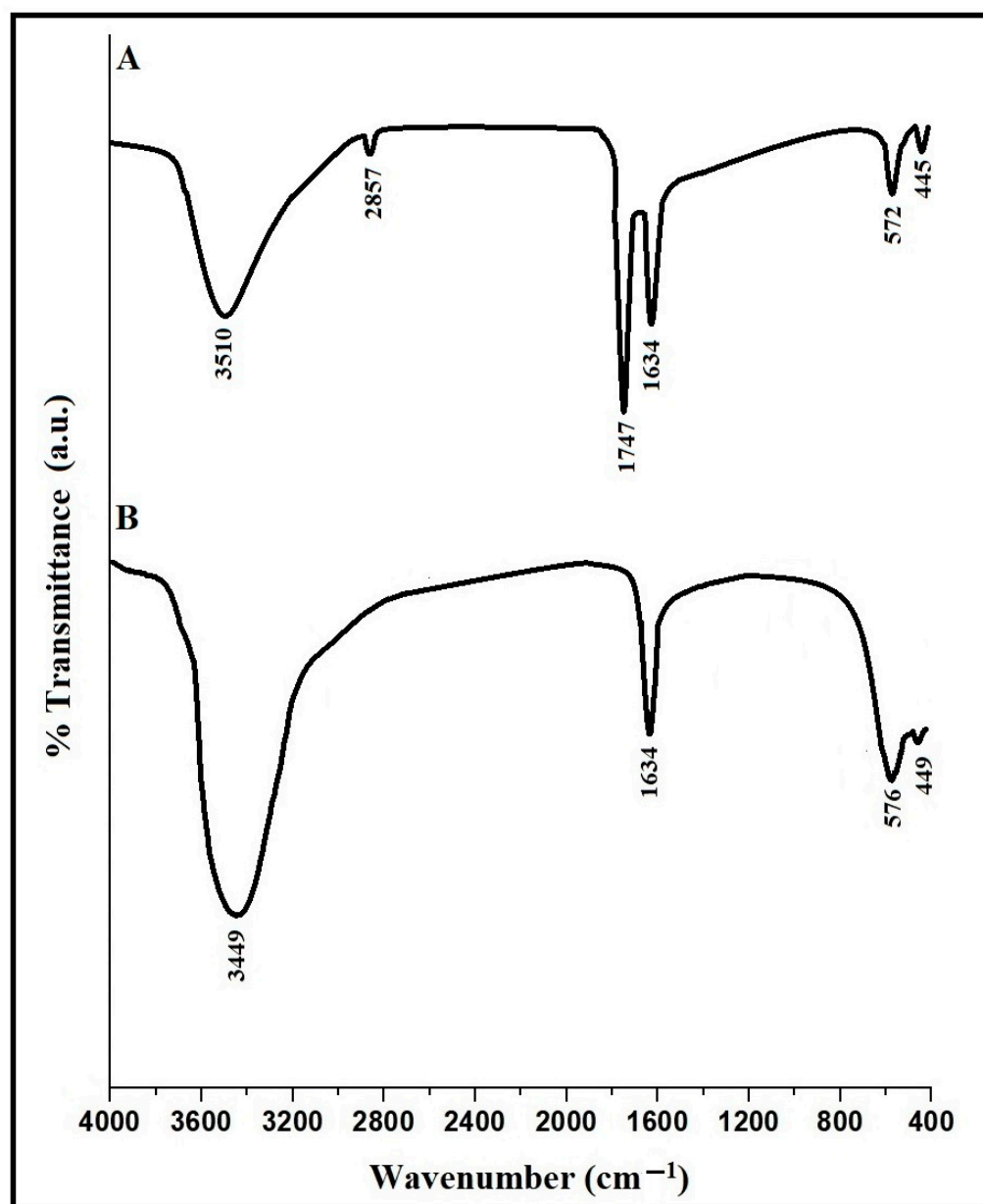
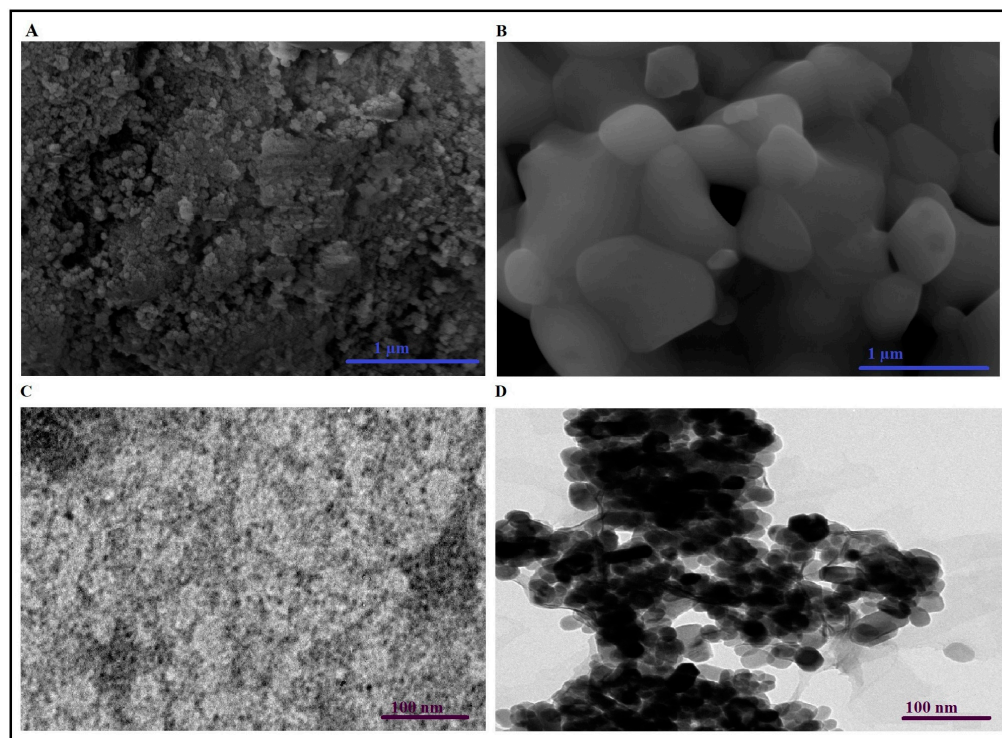


Figure 3. FTIR analysis of the uncalcinated (A) and calcinated (B) samples.

A scanning electron microscope was used to show the morphology of the uncalcinated and calcinated samples, as shown in Figure 4A,B, respectively. The results showed that the uncalcinated sample consists of amorphous forms, as shown in Figure 4A. Also, it can be noticed that  $\text{CaFe}_2\text{O}_4$  nanoparticles are nearly ball-like particles, with a mean grain size of 540.54 nm, as shown in Figure 4B. The analysis of the morphology of the uncalcinated and calcinated samples was conducted using a transmission electron microscope as shown in Figure 4C,D, respectively. The results displayed that the uncalcinated sample consists of amorphous forms, as presented in Figure 4C. Additionally, the  $\text{CaFe}_2\text{O}_4$  product revealed an aggregated spherical morphology with an average diameter of 27.48 nm, as presented in Figure 4D.



**Figure 4.** SEM analysis of the uncalcinated (A) and calcinated (B) samples. TEM analysis of the uncalcinated (C) and calcinated (D) samples.

The size obtained from scanning electron microscopy (SEM) analysis tends to be larger than that obtained from TEM analysis due to the difference in the depth of penetration of electron beams that is utilized in the two techniques. In SEM, the electron beam has a limited penetration depth, typically reaching only a few nanometers into the sample. This means that SEM predominantly captures surface features, which may be aggregates of several particles. In contrast, in TEM, the electron beam passes through the entire sample, allowing visualization of internal structures and providing more accurate measurements of particle size.

The Energy-dispersive X-ray spectroscopy (EDS) pattern, as shown in Figure 5, reveals that the  $\text{CaFe}_2\text{O}_4$  nanoparticles are composed of Ca, Fe, and O elements with an atomic ratio of 1:2:4 of the elements, respectively.

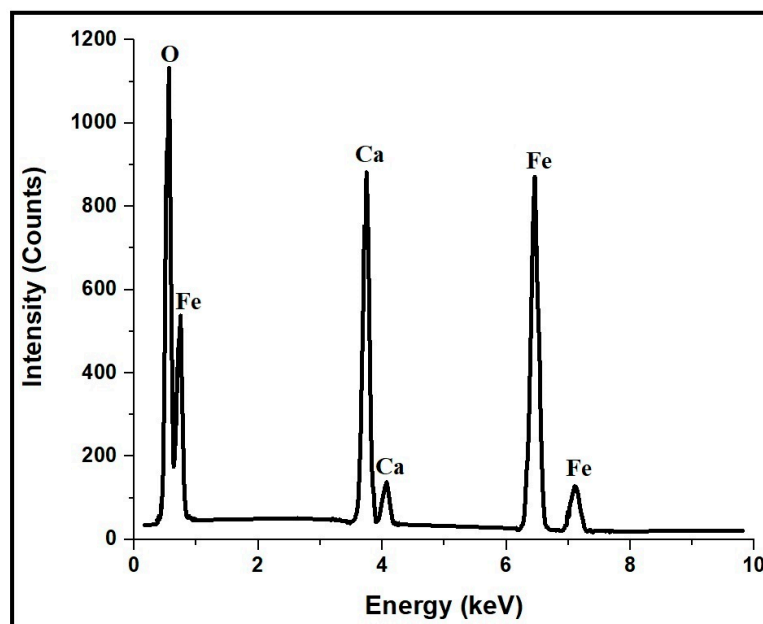


Figure 5. EDS spectrum of the  $\text{CaFe}_2\text{O}_4$  nanoparticles.

The magnetic properties of  $\text{CaFe}_2\text{O}_4$  nanoparticles were recorded at room temperature using a vibrating sample magnetometer, and the hysteresis curve of the  $\text{CaFe}_2\text{O}_4$  nanoparticles is shown in Figure 6. The results showed that the saturation magnetization is 36.65 emu/g.

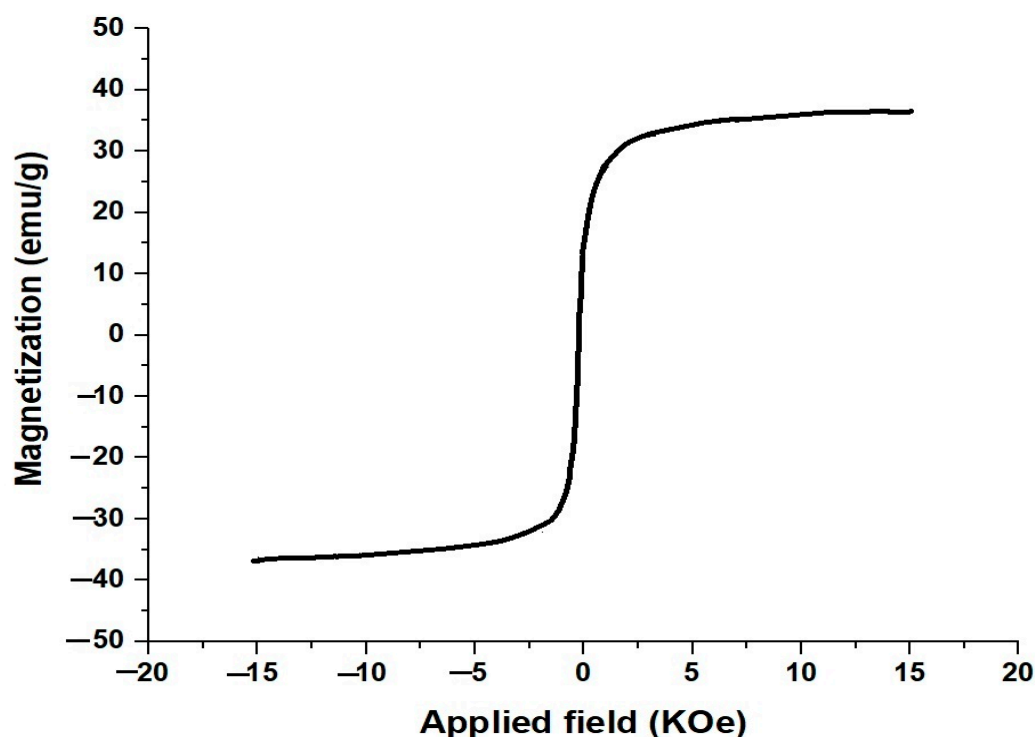


Figure 6. Magnetization curve of the  $\text{CaFe}_2\text{O}_4$  nanoparticles.

### 3.2. Removal of Congo Red Dye from Aqueous Media

#### 3.2.1. Effect of Dye Solution pH

Figure 7A illustrates the relationship between the removal percentage of Congo red dye and the pH of the dye solution. It was observed that the solution had a pH of 2,

resulting in the highest removal efficiency of 76.08%. As the solution pH increased, there was a consistent decrease in removal efficiency, with only 8.36% removal observed at pH 10. Accordingly, a pH of 2 was chosen as the ideal value for subsequent disposal studies. Figure 7B displays the point of zero charge of the  $\text{CaFe}_2\text{O}_4$  nanoparticles, which is 5.25. If the dye solution pH exceeds 5.25, the surface of  $\text{CaFe}_2\text{O}_4$  nanoparticles becomes negatively charged because of the existence of hydroxide ( $\text{OH}^-$ ) ions, leading to a repulsion force between the negatively charged Congo red dye and the negatively charged calcium ferrite surface. Hence, a noteworthy reduction is observed in removal efficiency [14,15]. On the contrary, if the solution pH is less than 5.25, the surface of  $\text{CaFe}_2\text{O}_4$  nanoparticles becomes positively charged because of the existence of positive hydrogen ( $\text{H}^+$ ) ions, leading to an attraction force between the negatively charged Congo red dye and the positively charged calcium ferrite surface. Hence, a noteworthy increase is observed in removal efficiency [14,15].

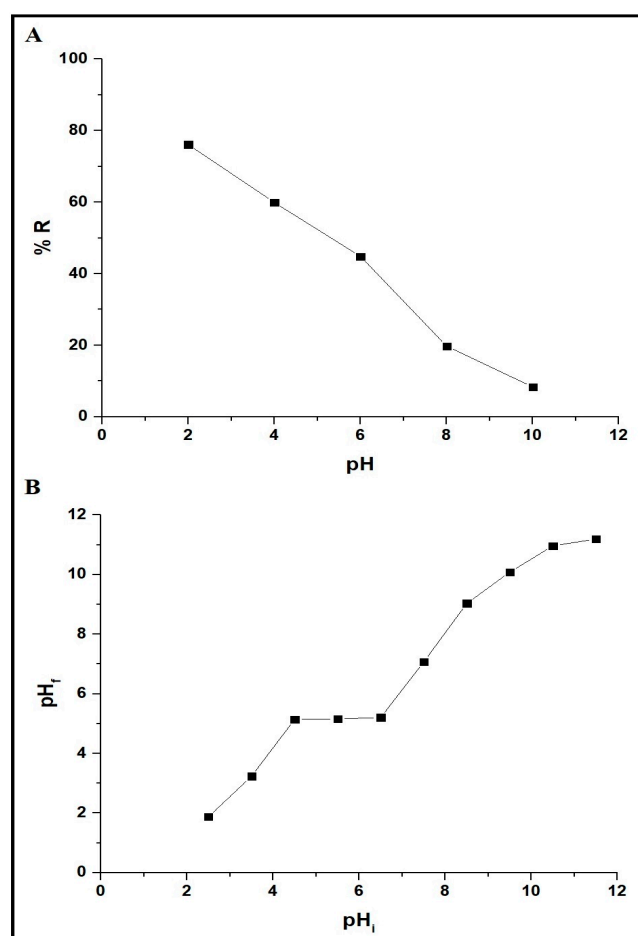


**Figure 7.** Variation of Congo red dye disposal efficiency (% R) versus pH (A). The point of zero charge of  $\text{CaFe}_2\text{O}_4$  nanoparticles (B).

The observation that the removal of Congo red dye is most efficient at pH 2 suggests that acidic conditions favor the adsorption of Congo red dye. This may be advantageous for water purification in terms of efficiency, but it raises concerns about the practical implementation and potential environmental impact. To address the issue of releasing highly acidic water into the environment after Congo red dye removal, neutralization process can be undertaken. The acidic water can be neutralized before discharge into the environment. This can be achieved by adding a base such as sodium hydroxide ( $\text{NaOH}$ ) or calcium hydroxide ( $\text{Ca}(\text{OH})_2$ ) to raise the pH to a more neutral level. Neutralization will ensure that the discharged water is less corrosive and less harmful to aquatic life.

Prior to Congo red dye adsorption, the  $\text{CaFe}_2\text{O}_4$  nanoparticles exhibited a total pore volume of 0.1307 cc/g and a BET surface area of 70.32  $\text{m}^2/\text{g}$ . Figure 8A,B shows the  $\text{N}_2$  adsorption/desorption isotherm of the  $\text{CaFe}_2\text{O}_4$  nanoparticles before and after the adsorption of Congo red dye, respectively. Following Congo red dye adsorption, the total pore volume and BET surface area of the  $\text{CaFe}_2\text{O}_4$  nanoparticles decreased to 0.0036 cc/g and 1.74  $\text{m}^2/\text{g}$ , respectively. This reduction is attributed to the blocking of pores in the  $\text{CaFe}_2\text{O}_4$  nanoparticles by Congo red dye molecules.

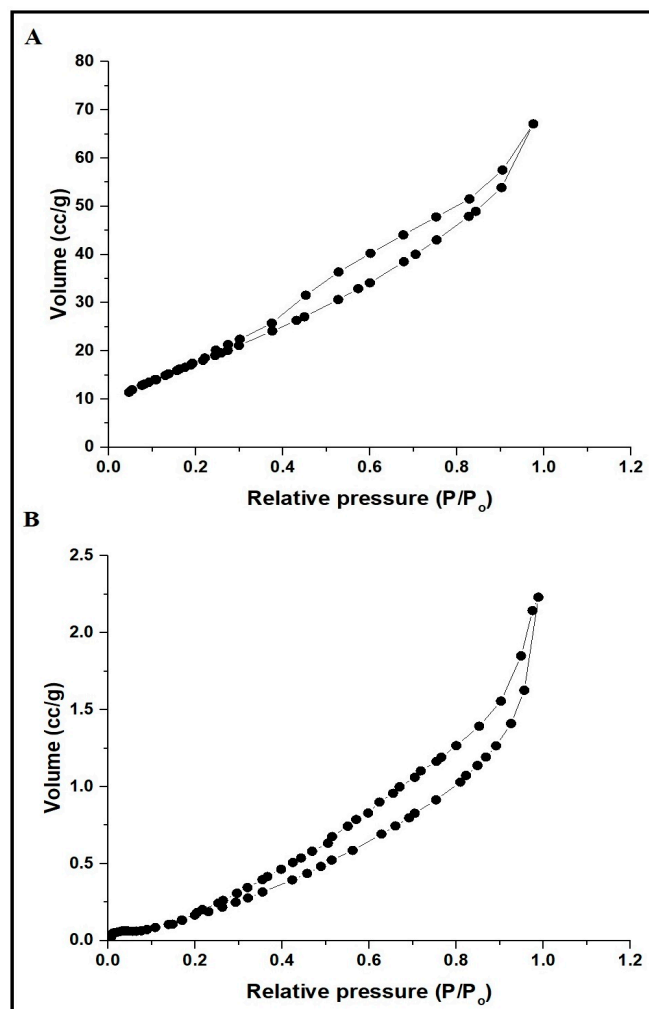


**Figure 8.**  $\text{N}_2$  adsorption/desorption isotherm of the  $\text{CaFe}_2\text{O}_4$  nanoparticles before (A) and after (B) the adsorption of Congo red dye.

### 3.2.2. Effect of Contact Time and Adsorption Kinetics

The variation of the removal percentage of Congo red dye as a function of contact time is displayed in Figure 9A. The results clearly demonstrate that the rate of removal was fast and the Congo red dye removal efficiency increased from 41.87 to 75.75% with increasing disposal time from 10 to 80 min due to the availability of positively charged  $\text{CaFe}_2\text{O}_4$  nanoparticles. Thereafter, the adsorption rate was slightly reduced with increasing removal time from 80 to 120 min due to equilibrium, which results from the fullness of active sites of  $\text{CaFe}_2\text{O}_4$  nanoparticles.

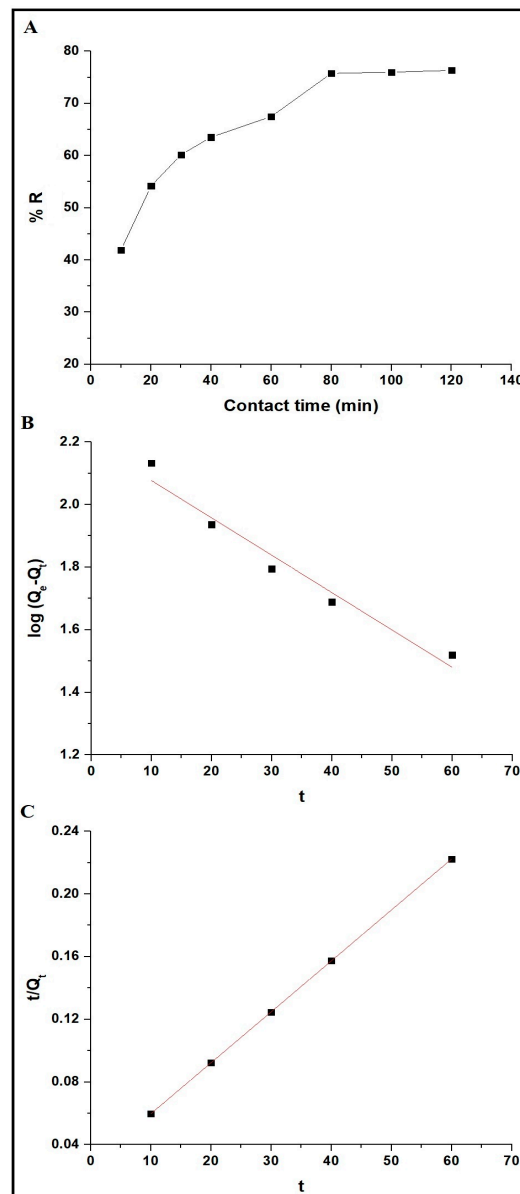


**Figure 9.** Variation of Congo red dye disposal efficiency (% R) versus contact time (A). The pseudo-first-order (B) and pseudo-second-order (C) models.

Pseudo-first-order typically indicates adsorption through a single-step process, while pseudo-second-order suggests adsorption involving chemisorption or strong physical interactions between the adsorbate and the adsorbent surface. If the adsorption follows a pseudo-first-order model, it means that the rate of adsorption is proportional to the difference between the equilibrium concentration of the adsorbate and the concentration at any given time. Also, if the adsorption follows a pseudo-second-order model, it means that the rate of adsorption is directly proportional to the square of the difference between the equilibrium concentration of the adsorbate and the concentration at any given time.

In this investigation, the kinetic study was examined using the pseudo-first-order and pseudo-second-order models. The linear forms of the previous kinetic models are presented in Equations (3) and (4), respectively [14,15,30–34].

$$\log(Q_e - Q_t) = \log Q_e - \frac{k_{First}}{2.303} t \quad (3)$$

$$\frac{t}{Q_t} = \frac{1}{k_{Second}Q_e^2} + \frac{1}{Q_e}t \quad (4)$$

where  $Q_t$  indicates the quantity of Congo red dye removed by the  $\text{CaFe}_2\text{O}_4$  nanoparticles at contact time  $t$  (mg/g),  $Q_e$  indicates the amount of Congo red dye removed by the  $\text{CaFe}_2\text{O}_4$  adsorbent at equilibrium time (mg/g),  $k_{First}$  indicates the pseudo-first-order model rate constant (1/min), and  $k_{Second}$  indicates the pseudo-second-order rate constant (g/mg·min). Additionally, Figure 9B illustrates the matching of kinetic experimental findings with the pseudo-second-order kinetic model. Also, Figure 9C illustrates the matching of kinetic experimental findings with the pseudo-second-order kinetic model. Table 1 provides the kinetic parameters of the applied models. Table 1 reveals that the  $R^2$  value of the pseudo-second-order model surpasses that of the pseudo-first-order model. Additionally, the comparison between the experimental disposal capacity ( $Q_{exp}$ ) and the model-calculated values unmistakably demonstrates a close agreement between the pseudo-second-order model adsorption capacity and the experimental adsorption capacity. Therefore, these findings indicate the suitability of the pseudo-second-order model for this disposal process, confirming the existence of chemisorption between Congo red dye and  $\text{CaFe}_2\text{O}_4$  nanoparticles.

**Table 1.** Kinetic constants of Congo red dye disposal by  $\text{CaFe}_2\text{O}_4$  nanoparticles.

Experimental $Q_{exp}$ (mg/g)	Pseudo-First-Order			Pseudo-Second-Order		
	$Q_e$ (mg/g)	$k_{First}$ (1/min)	$R^2$	$Q_e$ (mg/g)	$k_{Second}$ (g/mg·min)	$R^2$
$303 \pm 3.5$	$157.17 \pm 17.48$	$0.0275 \pm 0.0031$	0.9524	$307.69 \pm 0.26$	$0.00039 \pm 7.61 \times 10^{-7}$	0.9999

### 3.2.3. Effect of Solution Temperature and Thermodynamic Parameters

The variation of the removal percentage of Congo red dye as a function of temperature is presented in Figure 10A. The results clearly demonstrate that the Congo red dye uptake efficiency decreased from 75.75 to 27.70% with increasing disposal temperature from 298 to 328 K. The decrease in adsorption efficiency of Congo red dye using  $\text{CaFe}_2\text{O}_4$  nanoparticles with increasing temperature from 298 K to 328 K could be attributed to the desorption of Congo red dye from the surface of  $\text{CaFe}_2\text{O}_4$  nanoparticles. This means that as temperature rises, the equilibrium shifts towards desorption rather than adsorption.

Also, to investigate the effect of disposal temperature on the removal of Congo red dye by  $\text{CaFe}_2\text{O}_4$  nanoparticles, the standard entropy change ( $\Delta S^\circ$ ), standard enthalpy change ( $\Delta H^\circ$ ), and standard Gibbs free energy change ( $\Delta G^\circ$ ) were determined using Equations (5)–(7) [14,15,30–34].

$$\ln K_d = \frac{\Delta S^\circ}{R} - \frac{\Delta H^\circ}{RT} \quad (5)$$

$$\Delta G^\circ = \Delta H^\circ - T\Delta S^\circ \quad (6)$$

$$K_d = \frac{Q_e}{C_{eq}} \quad (7)$$

where  $T$  represents the disposal temperature (K),  $R$  indicates the universal gas constant (KJ/molK), and  $K_d$  represents the distribution coefficient (L/g). Also, the values of  $\Delta S^\circ$  and  $\Delta H^\circ$  were estimated from the intercept and slope of the plot of  $\ln K_d$  versus  $1/T$ , respectively, as shown in Figure 10B. The obtained thermodynamic constants are presented in Table 2. The  $\Delta G^\circ$  values are negative, and hence this confirms that the removal process of Congo red dye by  $\text{CaFe}_2\text{O}_4$  nanoparticles is spontaneous. The obtained  $\Delta H^\circ$  value (−56.30 KJ/mol) confirmed that the disposal process is exothermic. The obtained  $\Delta H^\circ$  value is more than 40 KJ/mol, which reveals that the removal process of Congo red dye is accomplished essentially by chemisorption. The positive value of  $\Delta S^\circ$  (0.1745 KJ/molK) is related to

a growth in the degree of mobility of the Congo red dye and signifies a growth in the concentration of Congo red dye at the solid–solution interface [14,15].

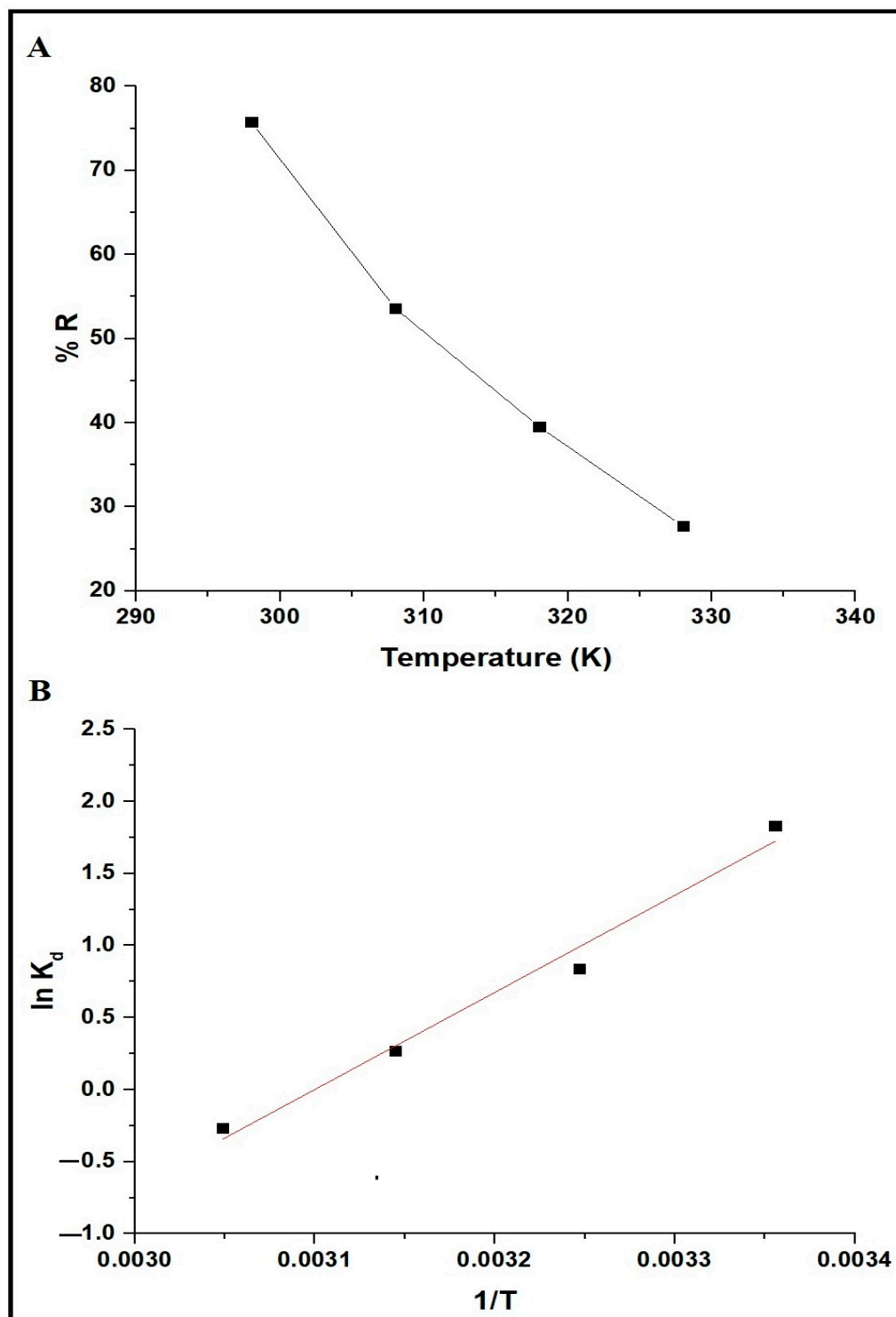


**Figure 10.** Variation of Congo red dye disposal efficiency (% R) versus temperature (A). The plot of  $\ln K_d$  against  $1/T$  (B).

**Table 2.** Thermodynamic constants of Congo red dye disposal by CaFe<sub>2</sub>O<sub>4</sub> nanoparticles.

$\Delta H^\circ$ (KJ/mol)	$\Delta S^\circ$ (KJ/mol K)	$\Delta G^\circ$ (KJ/mol)			
		298 K	308 K	318 K	328 K
$-56.30 \pm 5.29$	$0.1745 \pm 0.017$	$-108.31 \pm 10.35$	$-110.05 \pm 10.52$	$-111.79 \pm 10.68$	$-113.54 \pm 10.85$

### 3.2.4. Effect of Concentration and Adsorption Isotherms

The variation of the removal percentage of Congo red dye as a function of the initial dye concentration is presented in Figure 11A. The results clearly demonstrate that the Congo red dye removal efficiency decreased from 95.74 to 61.19% with a rise in the initial concentration of Congo red dye from 50 to 250 mg/L. Furthermore, this phenomenon could be ascribed to the existence of unsaturated active centers at smaller dye concentrations, whereas at greater Congo dye concentrations, it is possible that all the active centers become saturated.

In this investigation, the equilibrium study was conducted utilizing the Freundlich and Langmuir isotherms. The linear forms of the previous equilibrium isotherms are presented in Equations (8) and (9), respectively [14,15,30–34].

$$\frac{C_e}{Q_e} = \frac{1}{k_L Q_{max}} + \frac{C_e}{Q_{max}} \quad (8)$$

$$\ln Q_e = \ln k_F + \frac{1}{n} \ln C_{eq} \quad (9)$$

where  $1/n$  indicates the heterogeneity parameter,  $k_L$  indicates the Langmuir constant (L/mg),  $k_F$  indicates the Freundlich constant (mg/g)(L/mg)<sup>1/n</sup>, and  $Q_{max}$  indicates the maximum adsorption capacity of the Langmuir isotherm (mg/g). Additionally,  $Q_{max}$  can be determined from the Freundlich isotherm using Equation (10) [14,15,30–34].

$$Q_{max} = k_F \left( C_o^{1/n} \right) \quad (10)$$

Figure 11B illustrates the fitting of equilibrium experimental results with the Langmuir isotherm, whereas Figure 11C illustrates the fitting of equilibrium experimental results with the Freundlich isotherm. Table 3 provides the equilibrium constants of the applied isotherms. Table 3 reveals that the R<sup>2</sup> value of the Langmuir isotherm surpasses that of the Freundlich isotherm. Therefore, these outcomes indicate the suitability of the Langmuir isotherm for this disposal process.

**Table 3.** Equilibrium constants of Congo red dye disposal by CaFe<sub>2</sub>O<sub>4</sub> nanoparticles.

Langmuir Isotherm			Freundlich Isotherm		
$Q_{max}$ (mg/g)	$k_L$ (L/mg)	R <sup>2</sup>	$Q_{max}$ (mg/g)	$k_F$ (mg/g)(L/mg) <sup>1/n</sup>	R <sup>2</sup>
$318.55 \pm 6.17$	$0.3203 \pm 0.09$	0.9985	$574.76 \pm 409.95$	$107.11 \pm 29.20$	0.6619

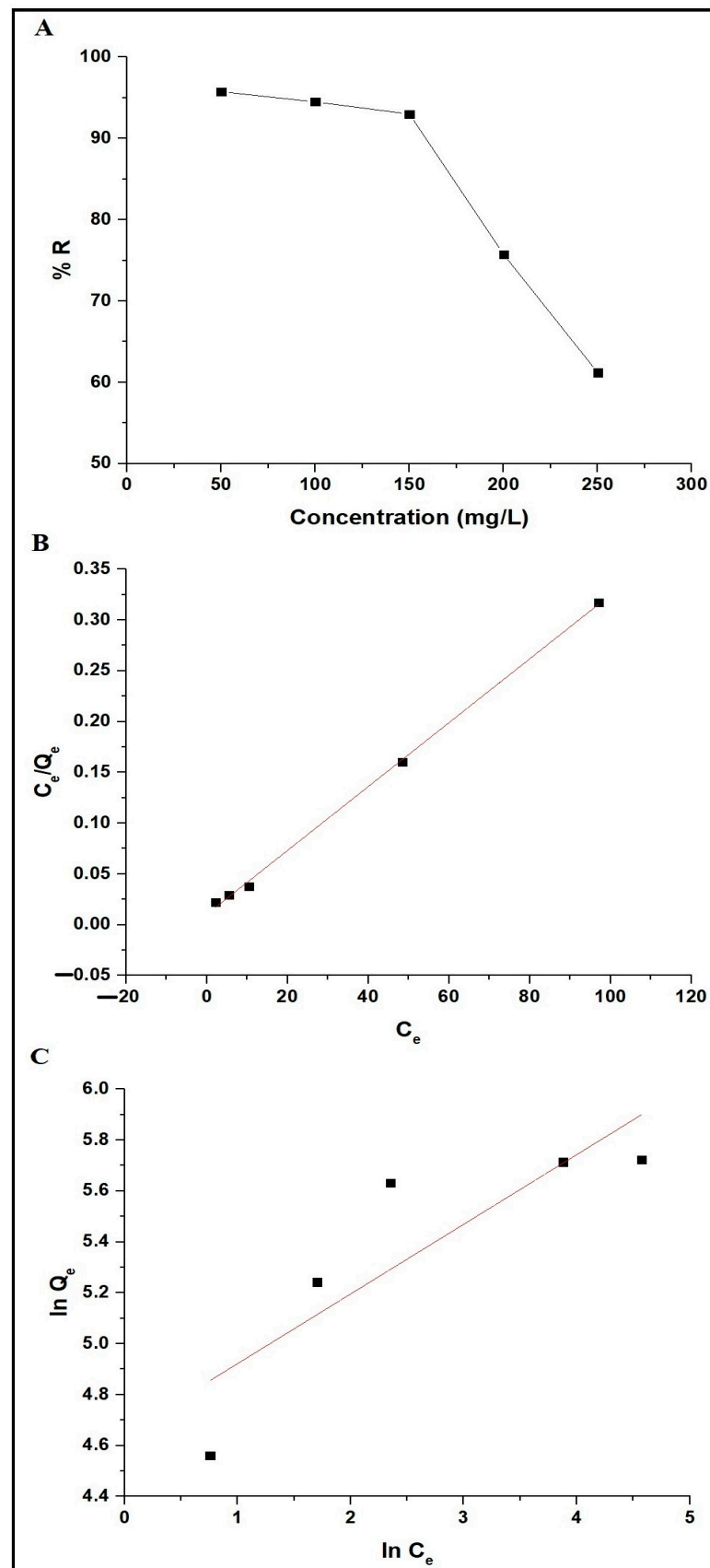


**Figure 11.** Variation of Congo red dye disposal efficiency (% R) versus the initial concentration of dye (A). The Langmuir (B) and Freundlich (C) isotherms.

The Langmuir isotherm analysis yielded a greatest disposal capacity of 318.47 mg/g for Congo red dye on  $\text{CaFe}_2\text{O}_4$  nanoparticles. During the assessment of the greatest disposal capacity, a comparison study was carried out between the disposal performance of Congo red dye on  $\text{CaFe}_2\text{O}_4$  nanoparticles and that of several adsorbents, as reported in Table 4. The results clearly demonstrate that the synthesized  $\text{CaFe}_2\text{O}_4$  nanoparticles exhibit a greater disposal capacity for Congo red dye when compared to formerly reported adsorbents such as activated carbon/chitosan composite,  $\text{ZnCr}_2\text{O}_4$  nanoparticles,  $\text{Fe}_3\text{O}_4$ /activated carbon composite, Mn/ZnO composite,  $\text{Fe}_3\text{O}_4$ /NiO composite, cationic surfactant-modified clinoptilolite, maghemite/polypyrrole composite, nanocellulose/polypyrrole composite, and  $\text{MgAl}_2\text{O}_4$  nanoparticles [40–48]. The higher adsorption performance of  $\text{CaFe}_2\text{O}_4$  nanoparticles towards Congo red dye compared to other adsorbents could be attributed to surface area and pH compatibility.  $\text{CaFe}_2\text{O}_4$  nanoparticles exhibit superior adsorption performance within an acidic pH, which is favorable for the removal of Congo red dye by the electrostatic attraction between the positively charged adsorbent surface and negatively charged Congo red dye. Also,  $\text{CaFe}_2\text{O}_4$  nanoparticles have a high surface area and pore volume, providing more active sites and increased accessibility for Congo red dye molecules to interact with the adsorbent surface.

**Table 4.** A comparison study between the greatest disposal capacity of  $\text{CaFe}_2\text{O}_4$  nanoparticles towards Congo red dye and that of other adsorbents.

Adsorbent	Maximum Disposal Capacity (mg/g)	Ref.
Activated carbon/chitosan composite	5.99	[40]
$\text{ZnCr}_2\text{O}_4$ nanoparticles	44.04	[41]
$\text{Fe}_3\text{O}_4$ /activated carbon composite	122.22	[42]
Mn/ZnO composite	232.50	[43]
$\text{Fe}_3\text{O}_4$ /NiO composite	89.90	[44]
Cationic surfactant-modified clinoptilolite	200.00	[45]
Maghemite/polypyrrole composite	269.50	[46]
Nanocellulose/polypyrrole composite	298.98	[47]
$\text{MgAl}_2\text{O}_4$ nanoparticles	24.50	[48]
$\text{CaFe}_2\text{O}_4$ nanoparticles	318.55	This study

The advantage of using  $\text{CaFe}_2\text{O}_4$  nanoparticles to remove dye from water lies in their ability to effectively sequester the pollutant from the aqueous solution. While it is true that the dye molecules will be adsorbed onto the surface of  $\text{CaFe}_2\text{O}_4$ , this method prevents water contamination. By removing the dye molecules from the water, the risk of contamination to aquatic ecosystems, wildlife, and human health is significantly reduced. This helps to maintain water quality and safeguard sensitive habitats from the adverse effects of dye pollution.

### 3.2.5. Effect of Regeneration and Reusability

$\text{CaFe}_2\text{O}_4$  adsorbent was regenerated by heating the  $\text{CaFe}_2\text{O}_4$ /Congo red dye mixture at 873 K to break down the dye and eliminate it. Afterward, the regenerated  $\text{CaFe}_2\text{O}_4$  adsorbent was employed for the elimination of Congo red dye in five consecutive cycles using the same previously described experimental method, as displayed in Figure 12. The results demonstrated the ability of  $\text{CaFe}_2\text{O}_4$  nanoparticles to remove Congo red dye several times, without its efficiency being significantly affected.

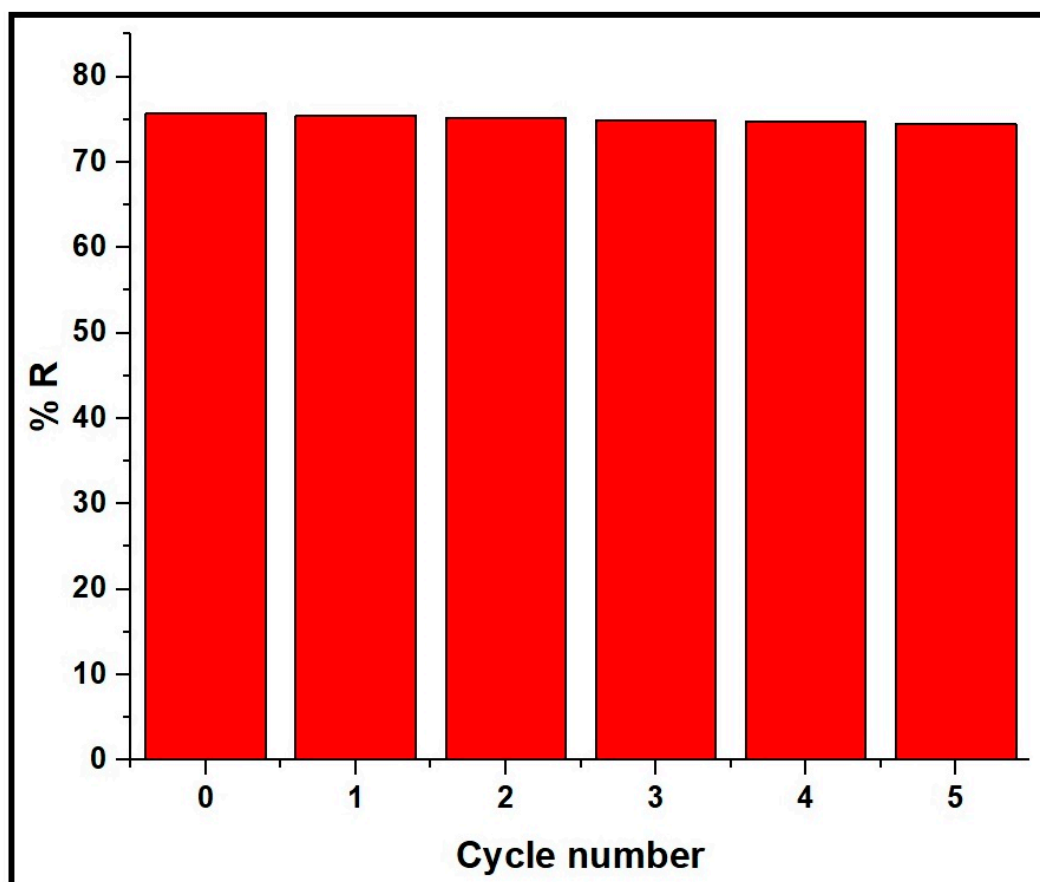


**Figure 12.** Effect the reusability of  $\text{CaFe}_2\text{O}_4$  nanoparticles on the elimination of Congo red dye. Experimental conditions: initial concentration of dye solution = 200 mg/L, volume of dye solution = 100 mL, amount of adsorbent = 0.05 g, pH = 2, temperature = 298 K, and contact time = 80 min.

After cycle 5, the adsorbent full of dye would typically be disposed of in accordance with proper waste management protocols. Depending on local regulations and the specific characteristics of the adsorbent material and the dye, disposal options may include landfill disposal. The adsorbent material, along with the adsorbed dye, may be disposed of in a licensed landfill facility. Proper containment measures should be employed to prevent the leaching of contaminants into the environment.

#### 4. Conclusions

This study involves the simple synthesis of  $\text{CaFe}_2\text{O}_4$  nanoparticles by the Pechini sol-gel method, which are subsequently utilized as an adsorbent for the efficient removal of Congo red dye from aqueous solutions. The maximum adsorption capacity of  $\text{CaFe}_2\text{O}_4$  for Congo red dye is 318.47 mg/g. Also, the XRD study showed that the mean crystal size of  $\text{CaFe}_2\text{O}_4$  nanoparticles is 24.34 nm. Examination by SEM reveals that the calcium ferrite nanoparticles exhibit approximate ball-like shapes with a mean grain size of 540.54 nm. Furthermore, TEM analysis demonstrates that the  $\text{CaFe}_2\text{O}_4$  nanoparticles exhibit aggregated spherical particles with a mean diameter of 27.48 nm. The removal of Congo red dye by  $\text{CaFe}_2\text{O}_4$  is found to be spontaneous, exothermic, chemical, and well described by the pseudo-second-order kinetic model and Langmuir equilibrium isotherm. The optimum conditions for the removal of Congo red dye by  $\text{CaFe}_2\text{O}_4$  nanoparticles are pH 2, 80 min contact time, and 298 K adsorption temperature.

**Author Contributions:** N.S.A.-K. (funding, research writing), G.M.A.-S. (writing the interpretation of nanoparticle characterization, funding), F.K.A. (writing the introduction, preparing figures and tables), R.K.S. (writing the interpretation of the kinetic study), F.A.S. (writing the interpretation of the thermodynamic study), A.M.M. (writing the interpretation of the equilibrium study), K.u.R. (writing the introduction, research review), L.K. (research review), E.A.A. (research writing, research review, idea, experimental work, analysis). All authors have read and agreed to the published version of the manuscript.

**Funding:** This research was funded by Princess Nourah bint Abdulrahman University Researchers Supporting Project number (PNURSP2024R85), Princess Nourah bint Abdulrahman University, Riyadh, Saudi Arabia.

**Data Availability Statement:** Data are contained within the article.

**Acknowledgments:** The authors are grateful to Princess Nourah bint Abdulrahman University, Riyadh, Saudi Arabia, for funding this work through Researchers Supporting Project number (PNURSP2024R85).

**Conflicts of Interest:** The authors confirm that there are no conflicts of interest for this work.

## References

1. Akrami, M.; Danesh, S.; Eftekhari, M. Comparative Study on the Removal of Cationic Dyes Using Different Graphene Oxide Forms. *J. Inorg. Organomet. Polym. Mater.* **2019**, *29*, 1785–1797. [[CrossRef](#)]
2. Ghiasi, E.; Malekzadeh, A. Removal of Various Textile Dyes Using LaMn(Fe)O<sub>3</sub> and LaFeMn<sub>0.5</sub>O<sub>3</sub> Nanoperovskites; RSM Optimization, Isotherms and Kinetics Studies. *J. Inorg. Organomet. Polym. Mater.* **2020**, *30*, 2789–2804. [[CrossRef](#)]
3. Pawariya, V.; De, S.; Dutta, J. Synthesis and Characterization of a New Developed Modified-Chitosan Schiff Base with Improved Antibacterial Properties for the Removal of Bismarck Brown R and Eosin Y Dyes from Wastewater. *Carbohydr. Polym. Technol. Appl.* **2023**, *6*, 100352. [[CrossRef](#)]
4. Ahmadian, M.; Jaymand, M. Interpenetrating Polymer Network Hydrogels for Removal of Synthetic Dyes: A Comprehensive Review. *Coord. Chem. Rev.* **2023**, *486*, 215152. [[CrossRef](#)]
5. Kausar, A.; Zohra, S.T.; Ijaz, S.; Iqbal, M.; Iqbal, J.; Bibi, I.; Nouren, S.; El Messaoudi, N.; Nazir, A. Cellulose-Based Materials and Their Adsorptive Removal Efficiency for Dyes: A Review. *Int. J. Biol. Macromol.* **2023**, *224*, 1337–1355. [[CrossRef](#)]
6. Micheletti, D.H.; da Silva Andrade, J.G.; Porto, C.E.; Alves, B.H.M.; de Carvalho, F.R.; Sakai, O.A.; Batistela, V.R. A Review of Adsorbents for Removal of Yellow Tartrazine Dye from Water and Wastewater. *Bioresour. Technol. Rep.* **2023**, *24*, 101598. [[CrossRef](#)]
7. Chen, D.; Cao, Y.; Chen, N.; Feng, P. Synthesis and Characterization of Cobalt Metal Organic Frameworks Prepared by Ultrasonic Wave-Assisted Ball Milling for Adsorptive Removal of Congo Red Dye from Aqueous Solutions. *J. Inorg. Organomet. Polym. Mater.* **2021**, *31*, 1231–1240. [[CrossRef](#)]
8. Mohammadi, S.Z.; Safari, Z.; Madady, N. Synthesis of Co<sub>3</sub>O<sub>4</sub>@SiO<sub>2</sub> Core/Shell-Nylon 6 Magnetic Nanocomposite as an Adsorbent for Removal of Congo Red from Wastewater. *J. Inorg. Organomet. Polym. Mater.* **2020**, *30*, 3199–3212. [[CrossRef](#)]
9. Liu, M.; Yin, W.; Zhao, T.L.; Yao, Q.Z.; Fu, S.Q.; Zhou, G.T. High-Efficient Removal of Organic Dyes from Model Wastewater Using Mg(OH)<sub>2</sub>-MnO<sub>2</sub> Nanocomposite: Synergistic Effects of Adsorption, Precipitation, and Photodegradation. *Sep. Purif. Technol.* **2021**, *272*, 118901. [[CrossRef](#)]
10. Munyai, S.; Tetana, Z.N.; Mathipa, M.M.; Ntsendwana, B.; Hintsho-Mbita, N.C. Green Synthesis of Cadmium Sulphide Nanoparticles for the Photodegradation of Malachite Green Dye, Sulfisoxazole and Removal of Bacteria. *Optik* **2021**, *247*, 167851. [[CrossRef](#)]
11. Ihaddaden, S.; Aberkane, D.; Boukerroui, A.; Robert, D. Removal of Methylene Blue (Basic Dye) by Coagulation-Flocculation with Biomaterials (Bentonite and Opuntia Ficus Indica). *J. Water Process Eng.* **2022**, *49*, 102952. [[CrossRef](#)]
12. Mcyotto, F.; Wei, Q.; Macharia, D.K.; Huang, M.; Shen, C.; Chow, C.W.K. Effect of Dye Structure on Color Removal Efficiency by Coagulation. *Chem. Eng. J.* **2021**, *405*, 126674. [[CrossRef](#)]
13. Rodrigues de Almeida, E.J.; Christofolletti Mazzeo, D.E.; Deroldo Sommaggio, L.R.; Marin-Morales, M.A.; Rodrigues de Andrade, A.; Corso, C.R. Azo Dyes Degradation and Mutagenicity Evaluation with a Combination of Microbiological and Oxidative Discoloration Treatments. *Ecotoxicol. Environ. Saf.* **2019**, *183*, 109484. [[CrossRef](#)] [[PubMed](#)]
14. Al-Wasidi, A.S.; Khairy, M.; Abdulkhair, B.Y.; Abdelrahman, E.A. Efficient Disposal of Basic Fuchsin Dye from Aqueous Media Using ZrO<sub>2</sub>/MgMn<sub>2</sub>O<sub>4</sub>/Mg(Mg<sub>0.333</sub>Mn<sub>1.333</sub>)O<sub>4</sub> as a Novel and Facilely Synthesized Nanocomposite. *Inorganics* **2023**, *11*, 363. [[CrossRef](#)]
15. Abdelrahman, E.A.; Algethami, F.K.; Alsalem, H.S.; Binkadem, M.S. Facile Synthesis and Characterization of Novel Nanostructures for the Efficient Disposal of Crystal Violet Dye from Aqueous Media. *Inorganics* **2023**, *11*, 339. [[CrossRef](#)]
16. Abdelrahman, E.A.; Algethami, F.K.; Alsalem, H.S.; Binkadem, M.S.; Khairy, M.; Saad, F.A.; El-Sayyad, G.S.; Alqahtani, Z. Efficient Disposal of Rhodamine 6G and Acid Orange 10 Dyes from Aqueous Media Using ZrO<sub>2</sub>/CdMn<sub>2</sub>O<sub>4</sub>/CdO as Novel and Facilely Synthesized Nanocomposites. *Inorganics* **2023**, *11*, 333. [[CrossRef](#)]

17. Salahshoori, I.; Namayandeh Jorabchi, M.; Ghasemi, S.; Mirnezami, S.M.S.; Nobre, M.A.L.; Khonakdar, H.A. Assessing Cationic Dye Adsorption Mechanisms on MIL-53 (Al) Nanostructured MOF Materials Using Quantum Chemical and Molecular Simulations: Toward Environmentally Sustainable Wastewater Treatment. *J. Water Process Eng.* **2023**, *55*, 104081. [[CrossRef](#)]
18. Nure, J.F.; Mengistu, A.; Abewaa, M.; Angassa, K.; Moyo, W.; Phiri, Z.; Mafa, P.J.; Kuvarega, A.T.; Nkambule, T.T.I. Adsorption of Black MNN Reactive Dye from Tannery Wastewater Using Activated Carbon of Rumex Abysinicus. *J. Taiwan Inst. Chem. Eng.* **2023**, *151*, 105138. [[CrossRef](#)]
19. Ji, Y.; Xu, F.; Wei, W.; Gao, H.; Zhang, K.; Zhang, G.; Xu, Y.; Zhang, P. Efficient and Fast Adsorption of Methylene Blue Dye onto a Nanosheet MFI Zeolite. *J. Solid State Chem.* **2021**, *295*, 121917. [[CrossRef](#)]
20. Duyar, C.; Pendar, A.; Bektaş, N.; Zorlu, Y.; Davarcı, D. 2D and 3D Ag(I) Coordination Polymers with a 2-Methylimidazole Substituted Cyclotriphosphazene Ligand: Structures and Dye Adsorption Properties. *Polyhedron* **2023**, *244*, 116589. [[CrossRef](#)]
21. Kanwal, A.; Bhatti, H.N.; Iqbal, M.; Noreen, S. Basic Dye Adsorption onto Clay/MnFe<sub>2</sub>O<sub>4</sub> Composite: A Mechanistic Study. *Water Environ. Res.* **2017**, *89*, 301–311. [[CrossRef](#)] [[PubMed](#)]
22. Adeogun, A.I. Removal of Methylene Blue Dye from Aqueous Solution Using Activated Charcoal Modified Manganese Ferrite (AC-MnFe<sub>2</sub>O<sub>4</sub>): Kinetics, Isotherms, and Thermodynamics Studies. *Part. Sci. Technol.* **2020**, *38*, 756–767. [[CrossRef](#)]
23. Hassan, M.R.; Aly, M.I. Magnetically Synthesized MnFe<sub>2</sub>O<sub>4</sub> Nanoparticles as an Effective Adsorbent for Lead Ions Removal from an Aqueous Solution. *Aqua Water Infrastruct. Ecosyst. Soc.* **2021**, *70*, 901–920. [[CrossRef](#)]
24. Algarni, T.S.; Al-Mohaimeed, A.M.; Al-Odayni, A.B.; Abduh, N.A.Y. Activated Carbon/ZnFe<sub>2</sub>O<sub>4</sub> Nanocomposite Adsorbent for Efficient Removal of Crystal Violet Cationic Dye from Aqueous Solutions. *Nanomaterials* **2022**, *12*, 3224. [[CrossRef](#)]
25. Vergis, B.R.; Kottam, N.; Hari Krishna, R.; Nagabushana, B.M. Removal of Evans Blue Dye from Aqueous Solution Using Magnetic Spinel ZnFe<sub>2</sub>O<sub>4</sub> Nanomaterial: Adsorption Isotherms and Kinetics. *Nano-Struct. Nano-Objects* **2019**, *18*, 100290. [[CrossRef](#)]
26. Gupta, A.; Viltres, H.; Gupta, N.K. Sono-Adsorption of Organic Dyes onto CoFe<sub>2</sub>O<sub>4</sub>/Graphene Oxide Nanocomposite. *Surf. Interfaces* **2020**, *20*, 100563. [[CrossRef](#)]
27. Wu, X.; Wang, W.; Li, F.; Khaimanov, S.; Tsidaeva, N.; Lahoubi, M. PEG-Assisted Hydrothermal Synthesis of CoFe<sub>2</sub>O<sub>4</sub> Nanoparticles with Enhanced Selective Adsorption Properties for Different Dyes. *Appl. Surf. Sci.* **2016**, *389*, 1003–1011. [[CrossRef](#)]
28. Adel, M.; Ahmed, M.A.; Mohamed, A.A. Synthesis and Characterization of Magnetically Separable and Recyclable Crumbled MgFe<sub>2</sub>O<sub>4</sub>/Reduced Graphene Oxide Nanoparticles for Removal of Methylene Blue Dye from Aqueous Solutions. *J. Phys. Chem. Solids* **2021**, *149*, 109760. [[CrossRef](#)]
29. Al-Wasidi, A.S.; Algethami, F.K.; Saad, F.A.; Abdelrahman, E.A. Remarkable High Adsorption of Methylene Blue Dye from Aqueous Solutions Using Facilely Synthesized MgFe<sub>2</sub>O<sub>4</sub> Nanoparticles. *J. Inorg. Organomet. Polym. Mater.* **2023**, *33*, 2035–2045. [[CrossRef](#)]
30. Kazemi, J.; Javanbakht, V. Alginate Beads Impregnated with Magnetic Chitosan@Zeolite Nanocomposite for Cationic Methylene Blue Dye Removal from Aqueous Solution. *Int. J. Biol. Macromol.* **2020**, *154*, 1426–1437. [[CrossRef](#)] [[PubMed](#)]
31. Patel, P.K.; Pandey, L.M.; Uppaluri, R.V.S. Synthesized Carboxymethyl-Chitosan Variant Composites for Cyclic Adsorption-Desorption Based Removal of Fe, Pb, and Cu. *Chemosphere* **2023**, *340*, 139780. [[CrossRef](#)]
32. Hassan, S.S.M.; El-Aziz, M.E.A.; Fayez, A.E.S.; Kamel, A.H.; Youssef, A.M. Synthesis and Characterization of Bio-Nanocomposite Based on Chitosan and CaCO<sub>3</sub> Nanoparticles for Heavy Metals Removal. *Int. J. Biol. Macromol.* **2024**, *255*, 128007. [[CrossRef](#)]
33. Kenawy, I.M.M.; Abou El-Reash, Y.G.; Hassaniien, M.M.; Alnagar, N.R.; Mortada, W.I. Use of Microwave Irradiation for Modification of Mesoporous Silica Nanoparticles by Thioglycolic Acid for Removal of Cadmium and Mercury. *Microporous Mesoporous Mater.* **2018**, *258*, 217–227. [[CrossRef](#)]
34. Bingül, Z. Determination of Affecting Parameters on Removal of Methylene Blue Dye from Aqueous Solutions Using Natural Clay: Isotherm, Kinetic, and Thermodynamic Studies. *J. Mol. Struct.* **2022**, *1250*, 131729. [[CrossRef](#)]
35. Abdelrahman, E.A.; Khalil, M.M.H.; Algethami, F.K.; Khairy, M.; Abou El-Reash, Y.G.; Saad, F.A.; Shah, R.K.; Ammar, A.M. Facile Synthesis of MgO/CuO and MgO/Cu<sub>3</sub>MgO<sub>4</sub> Binary Nanocomposites as Promising Adsorbents for the Disposal of Zn(II) Ions. *J. Inorg. Organomet. Polym. Mater.* **2023**, *34*, 266–281. [[CrossRef](#)]
36. Manohar, A.; Krishnamoorthi, C. Structural, Optical, Dielectric and Magnetic Properties of CaFe<sub>2</sub>O<sub>4</sub> Nanocrystals Prepared by Solvothermal Reflux Method. *J. Alloys Compd.* **2017**, *722*, 818–827. [[CrossRef](#)]
37. Josun, J.; Sharma, P.; Kumar Garg, V. Optical and Structural Behavior of Hydrothermally Synthesized ZnO Nanoparticles at Various Temperatures with NaOH Molar Ratios. *Results Opt.* **2024**, *14*, 100601. [[CrossRef](#)]
38. Abdelrahman, E.A.; Al-Farraj, E.S. Facile Synthesis and Characterizations of Mixed Metal Oxide Nanoparticles for the Efficient Photocatalytic Degradation of Rhodamine B and Congo Red Dyes. *Nanomaterials* **2022**, *12*, 3992. [[CrossRef](#)]
39. Abdelrahman, E.A.; Hegazey, R.M.; Ismail, S.H.; El-Feky, H.H.; Khedr, A.M.; Khairy, M.; Ammar, A.M. Facile Synthesis and Characterization of β-Cobalt Hydroxide/Hydrohausmannite/Ramsdellite/Spertiniite and Tenorite/Cobalt Manganese Oxide/Manganese Oxide as Novel Nanocomposites for Efficient Photocatalytic Degradation of Methylene Blue Dye. *Arab. J. Chem.* **2022**, *15*, 104372. [[CrossRef](#)]
40. Jeyaseelan, C.; Kaur, M.; Sen, M. Activated Carbon Modified Chitosan Beads: An Effective Method for Removal of Congo Red Dye. *Mater. Today Proc.* **2023**. *In Press*. [[CrossRef](#)]

41. Gao, H.J.; Wang, S.F.; Fang, L.M.; Sun, G.A.; Chen, X.P.; Tang, S.N.; Yang, H.; Sun, G.Z.; Li, D.F. Nanostructured Spinel-Type  $M(M=Mg,Co,Zn)Cr_2O_4$  Oxides: Novel Adsorbents for Aqueous Congo Red Removal. *Mater. Today Chem.* **2021**, *22*, 100593. [[CrossRef](#)]
42. Priyan, V.V.; Kumar, N.; Narayanasamy, S. Toxicological Assessment and Adsorptive Removal of Lead (Pb) and Congo Red (CR) from Water by Synthesized Iron Oxide/Activated Carbon ( $Fe_3O_4/AC$ ) Nanocomposite. *Chemosphere* **2022**, *294*, 133758. [[CrossRef](#)]
43. Singh, N.; Shah, K.; Pramanik, B.K. Synthesis and Application of Manganese-Doped Zinc Oxide as a Potential Adsorbent for Removal of Congo Red Dye from Wastewater. *Environ. Res.* **2023**, *233*, 116484. [[CrossRef](#)]
44. Koochi, P.; Rahbar-kelishami, A.; Shayesteh, H. Efficient Removal of Congo Red Dye Using  $Fe_3O_4/NiO$  Nanocomposite: Synthesis and Characterization. *Environ. Technol. Innov.* **2021**, *23*, 101559. [[CrossRef](#)]
45. Nodehi, R.; Shayesteh, H.; Kelishami, A.R. Enhanced Adsorption of Congo Red Using Cationic Surfactant Functionalized Zeolite Particles. *Microchem. J.* **2020**, *153*, 104281. [[CrossRef](#)]
46. Ramírez-Ortega, A.A.; Medina-Llamas, M.; da Silva, R.J.; García-Elías, J.; de Lira-Gómez, P.; Medina-Llamas, J.C.; Chávez-Guajardo, A.E. Synthesis of a Maghemite-Polypyrrole Nanocomposite for the Removal of Congo Red Dye from Aqueous Solutions. *Environ. Nanotechnol. Monit. Manag.* **2021**, *16*, 100597. [[CrossRef](#)]
47. Shahnaz, T.; Padmanaban, V.C.; Narayanasamy, S. Surface Modification of Nanocellulose Using Polypyrrole for the Adsorptive Removal of Congo Red Dye and Chromium in Binary Mixture. *Int. J. Biol. Macromol.* **2020**, *151*, 322–332. [[CrossRef](#)]
48. Tatarchuk, T.; Myslin, M.; Mironyuk, I.; Kosobucki, P.; Scigalski, P.; Kotsyubynsky, V. Removal of Congo Red Dye, Polar and Non-Polar Compounds from Aqueous Solution Using Magnesium Aluminate Nanoparticles. *Mater. Today Proc.* **2019**, *35*, 518–522. [[CrossRef](#)]

**Disclaimer/Publisher's Note:** The statements, opinions and data contained in all publications are solely those of the individual author(s) and contributor(s) and not of MDPI and/or the editor(s). MDPI and/or the editor(s) disclaim responsibility for any injury to people or property resulting from any ideas, methods, instructions or products referred to in the content.